alkenones advected by deep waters originating from high northern latitudes is thus very unlikely. A similar argument can be made against a significant contribution of NADW to the concentration of fine-grained magnetite as could occur in sediments farther north (*46*).
20. The IRD studied at DGO (Talence, France) are expressed in number per gram for the size fraction greater than 150 μm (sample size for counting is 10 g of dry sediments). The complexity of H1 and H2 is further demonstrated by their mineralogical composition: The H2a IRD peak centered at 23,000 cal yr B.P. is characterized by a dominance of quartz (84%), with a presence of feldspars (5%), detrital carbonates (3%), and hematite-coated grains (2%). Broadly similar, the H1a IRD peak at 16,000 cal yr B.P. is dominated by grains of quartz (76%) and feldspars (14%), with small percentages of hematite-coated grains (3%), glauconite (3%), volcanic shards (1%), and an almost complete lack of detrital carbonate. By contrast, the smaller IRD peak at 17,500 cal yr B.P. (H1b) is composed mainly of detrital carbonates (80%), with secondary contributions of quartz (16%) and feldspar (3%).
21. N. Thouveny *et al.*, *Earth Planet. Sci. Lett.* **180**, 61 (2000).
22. S. M. Lebreiro, J. C. Moreno, I. N. McCave, P. P. E. Weaver, *Mar. Geol.* **131**, 47 (1996).
23. M. R. Chapman and N. J. Shackleton, *Earth Planet. Sci. Lett.* **159**, 57 (1998).
24. R. Zahn *et al.*, *Paleoceanography* **12**, 696 (1997).
25. M. Zhao, N. A. S. Beveridge, N. J. Shackleton, M. Sarnthein, G. Eglinton, *Paleoceanography* **10**, 661 (1995).
26. A. Rosell-Melé, G. Eglinton, U. Pflaumann, M. Sarnthein, *Geochim Cosmochim Acta* **59**, 3099 (1995).
27. S. C. Brassell, G. Eglinton, I. T. Marlowe, U. Pflaumann, M. Sarnthein, *Nature* **320**, 129 (1986).
28. E. L. Sikes, J. K. Volkman, L. G. Robertson, J.-J. Pichon, *Geochim. Cosmochim. Acta* **61**, 1495 (1997).
29. A. Rosell-Melé, *Paleoceanography* **13**, 694 (1998).
30. H.-M. Schulz, A. Schöner, K. C. Emeis, *Geochim. Cosmochim. Acta* **64**, 469 (2000).
31. J. C. Duplessy, E. Bard, L. Labeyrie, J. Duprat, J. Moyes, *Paleoceanography* **8**, 341 (1993).
32. M. R. Chapman and M. A. Maslin, *Geology* **27**, 875 (1999).
33. R. H. Gwiazda, S. R. Hemming, W. S. Broecker, *Paleoceanography* **11**, 371 (1996).
34. T. A. Mashiotta, D. W. Lea, H. J. Spero, *Earth Planet. Sci. Lett.* **170**, 417 (1999).
35. M. Stuiver *et al.*, *Radiocarbon* **40**, 1041 (1998).
36. E. Bard, M. Arnold, B. Hamelin, N. Tisnerat-Laborde, G. Cabioch, *Radiocarbon* **40**, 1085 (1998).
37. E. Bard *et al.*, *Earth Planet. Sci. Lett.* **126**, 275 (1994).
38. T. F. Stocker and D. G. Wright, *Radiocarbon* **40**, 359 (1998).
39. C. Sonzogni *et al.*, *Deep-Sea Res. II* **44**, 1445 (1997).
40. F. G. Prahl, L. A. Muehlhausen, D. L. Zahnle, *Geochim. Cosmochim. Acta* **52**, 2303 (1988).
41. P. J. Müller, G. Kirst, G. Ruhland, I. von Storch, A. Rosell-Melé, *Geochim. Cosmochim. Acta* **62**, 1757 (1998).
42. P. P. E. Weaver *et al.*, *Paleoceanography* **14**, 336 (1999).
43. A. Rosell-Melé and P. Comes, *Paleoceanography* **14**, 770 (1999).
44. J. Schönfeld and R. Zahn, *Palaeogeogr. Palaeoclimatol. Palaeoecol.* **159**, 85 (2000).
45. L. D. Keigwin and S. J. Lehman, *Paleoceanography* **9**, 185 (1994).
46. T. M. Dokken and E. Jansen, *Nature* **401**, 458 (1999).
47. We acknowledge helpful discussions or reviews by G. C. Bond, C. De La Rocha, R. Rickaby, A. Rosell-Melé, E. L. Sikes, N. Thouveny, and anonymous referees. We thank J.-J. Motte for drawing Fig. 1. This work is supported by CNRS Programme National d'Etudes de la Dynamique et du Climat and the European Community (projects ENV4-CT97-0564, FMRX-CT96-0046, and ENV4-CT97-0659).

22 March 2000; accepted 16 June 2000

Discrete Atom Imaging of One-Dimensional Crystals Formed Within Single-Walled Carbon Nanotubes

Rüdiger R. Meyer,[1] Jeremy Sloan,[2]* Rafal E. Dunin-Borkowski,[3] Angus I. Kirkland,[1,4] Miles C. Novotny,[2] Sam R. Bailey,[2] John L. Hutchison,[3] Malcolm L. H. Green[2]

The complete crystallography of a one-dimensional crystal of potassium iodide encapsulated within a 1.6-nanometer-diameter single-walled carbon nanotube has been determined with high-resolution transmission electron microscopy. Individual atoms of potassium and iodine within the crystal were identified from a phase image that was reconstructed with a modified focal series restoration approach. The lattice spacings within the crystal are substantially different from those in bulk potassium iodide. This is attributed to the reduced coordination of the surface atoms of the crystal and the close proximity of the van der Waals surface of the confining nanotube.

The synthesis and characterization of one-dimensional (1D) crystals that have a well-specified chemistry, size, and crystal structure have presented a formidable challenge for materials chemistry and analysis. Here, we show that both the widths and the lattice spacings of 1D crystals can be tailored by encapsulating them within single-walled carbon nanotubes (SWNTs) (*1*). The resulting crystals can be tens of micrometers in length yet only two or three atoms in width. We illustrate our results for a <110> projection of a discrete KI crystal that is three atomic layers thick and formed within a SWNT, in which the crystal thickness varies in a strictly integral fashion on an atomic scale.

Conventional high-resolution transmission electron microscopy (HRTEM) has previously been used to image single heavy atoms on crystal surfaces and amorphous support films (*2–6*). The technique can be applied in the same way to provide structural information about a crystal incorporated within a SWNT. However, the image contrast is weak and noisy, and it is, in general, only possible to identify strongly scattering species such as I in an encapsulated KI crystal (see below). A single HRTEM image is also subject to artifacts due to lens aberrations such as defocus, astigmatism, and beam tilt, particularly near the edge of a crystal. These problems can be overcome by recovering the amplitude and phase of the electron wave function at the exit surface of a sample from either a focal (*7–9*) or a tilt azimuth (*10, 11*) series of images. The procedure involves the determination of the lens aberrations and a numerical reconstruction of the exit plane wave function by using a Wiener filter. The restored wave function can then be used to calculate the high-spatial-frequency components of the phase shift of the electron wave as it leaves the sample. This phase image is free of artifacts introduced by objective lens aberrations and is higher in resolution and less noisy than an individual HRTEM image. It is also less noisy than an equivalent atomic resolution phase image obtained by electron holography (*12*). For a sufficiently thin crystal, the recorded phase can be interpreted intuitively because it is directly proportional to the projected potential of the sample integrated in the incident beam direction (*13*). However, the technique imposes strict requirements on specimen and instrumental stability and must be applied with great care to SWNTs, which are damaged readily by overexposure to a high-energy electron beam.

SWNTs were synthesized with a modified high-yield arc synthesis technique (*14*) and filled with highly pure KI (99.99%) (Aldrich) through a capillary filling method (*1, 15*). The specimen was characterized at 300 kV in a Japan Electron Optics Laboratory (JEOL) JEM-3000F field emission gun transmission electron microscope (*16–18*). Figure 1A shows a phase image reconstructed from a 20-member focal series of a 1.6-nm-diameter SWNT containing a KI single crystal (*19*). In cross section, the encapsulated crystal can be regarded as a single KI unit cell viewed along

[1]Department of Materials Science, University of Cambridge, Pembroke Street, Cambridge CB2 3QZ, UK. [2]Wolfson Catalysis Centre (Carbon Nanotechnology Group), Inorganic Chemistry Laboratory, University of Oxford, South Parks Road, Oxford OX1 3QR, UK. [3]Department of Materials, University of Oxford, Parks Road, Oxford OX1 3PH, UK. [4]Department of Chemistry, University of Cambridge, Lensfield Road, Cambridge CB2 1EW, UK.

*To whom correspondence should be addressed. E-mail: jeremy.sloan@chem.ox.ac.uk

the <110> direction of the parent rock salt structure, with the <001> direction parallel to the tube axis. The crystal is well resolved in regions 1 and 3 of the restoration, whereas in region 2, the crystal is rotated about its axis. Similar crystals were found in 30 to 50% of all SWNTS examined in this sample, although not all were oriented along a KI<110> direction.

In this projection, each white spot corresponds to a column of pure I or pure K that is exactly one, two, or three atoms in thickness, as can be seen in the enlargement of region 1 (upper left inset of Fig. 1A). The different phase shifts arising from different atomic columns are visible when region 1 is displayed as a surface plot (lower right inset of Fig. 1A). Corresponding line profiles across the phase image (Fig. 1, B to F) were obtained from the single-pixel line traces marked in the upper left inset of Fig. 1A. Along the center of the crystal (Fig. 1B), the contrast alternates between that of three K and three I atoms in projection, with the I columns giving rise to the higher peaks. Perpendicular to the length of the crystal, successive {001} layers alternate in a bimodal fashion between 1I-2K-3I-2K-1I (Fig. 1C) and 1K-2I-3K-2I-1K (Fig. 1D). The diagonal slices through the crystal (Fig. 1, E and F) correspond to projections of 1I-2I-3I-2I-1I and 1K-2K-3K-2K-1K {2-22} layers, respectively. The peak heights in Fig. 1, E and F, vary in an integral manner from peak to peak. The phase shifts of individual I and K atoms in the reconstructed image are ~0.06 and ~0.03 rad, respectively.

Scherzer defocus and reconstructed amplitude images are shown in Fig. 2, A and B, respectively. The signal in Fig. 2A is very noisy and originates primarily from the more strongly scattering I lattice, whereas the low contrast in Fig. 2B is consistent with the fact that the crystal is almost a pure phase object. Neither image can be used to obtain the quantitative information that can be provided by the reconstructed phase image. The energy-dispersive x-ray (EDX) spectrum (Fig. 2C), which was obtained from the crystal after imaging, provides confirmation of the presence of K and I in the filling material.

A multislice simulation of a phase image of a KI<110> crystal encapsulated within a 1.6-nm-diameter SWNT was performed (Fig. 3A). The factors that limit the resolution of the experimental reconstruction (temporal and spatial coherence and vibration) are not easy to quantify; Fig. 3A was therefore calculated on the assumption of no beam convergence, focal spread, or vibration and then smoothed with an identical Wiener filter to that applied to the experimental data. Atom positions corresponding to a (12,12) SWNT were used because it has the same diameter as the SWNT imaged in Fig. 1A (*20*). However, our experimental images are not sensitive to the conformation of the SWNT, and either "zigzag" (21,0) or chiral [for example, (*11, 13*)] tubules could have been chosen.

Line profiles (Fig. 3, B to F) were obtained from single-pixel line traces labeled B through F in Fig. 3A. The excellent visual agreement between the experimental and simulated line profiles supports the interpretation of the results. The magnitudes of the simulated phase shifts are about two times higher in the simulations than in the experimental data, despite the fact that the experimental crystal thickness was known exactly. This difference may provide insight into the similar (and poorly understood) discrepancy between the contrast of simulated and experimental conventional HRTEM images (*21*). It cannot be explained by including ionic scattering factors in the simulations.

Close inspection of Fig. 1A reveals a lattice distortion of the KI crystal that is not readily discernible in the corresponding HRTEM image taken at Scherzer defocus (Fig. 2A). Experimental measurements of lattice spacings in the crystal (Fig. 4) show a longitudinal contraction of the KI crystal from 0.705 to 0.695 nm along <001> (*22*), whereas in cross section, there is an expan-

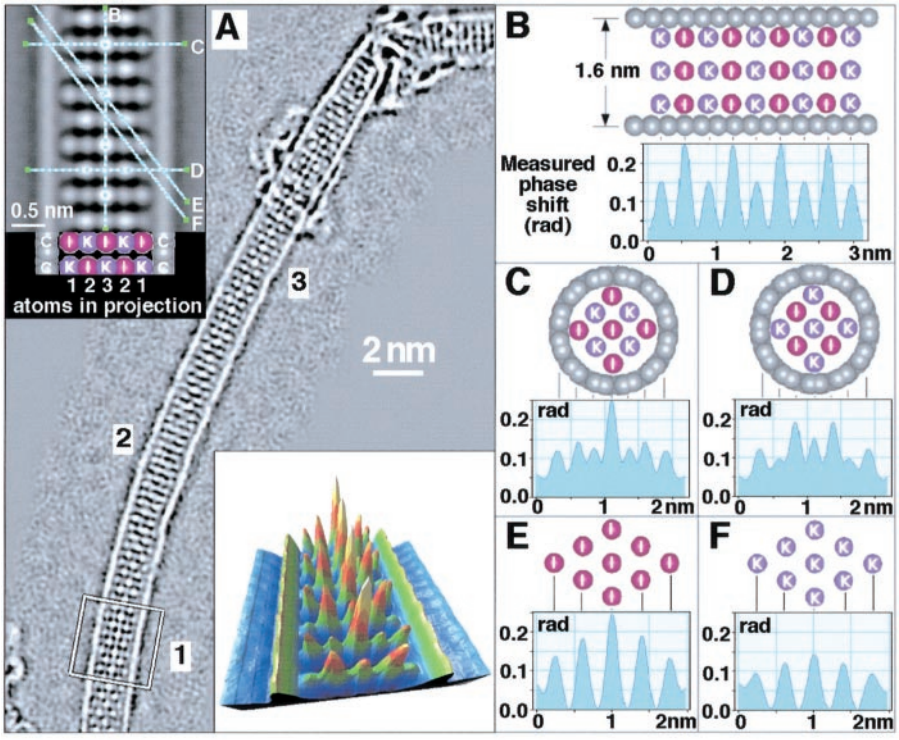

Fig. 1. (**A**) Phase image showing a <110> projection of KI incorporated within a 1.6-nm-diameter SWNT, reconstructed from a focal series of 20 images. Maximum and minimum spatial frequencies of 1/(0.23 nm) and 1/(1.05 nm), respectively, have been retained with a Wiener filter. The upper left inset shows an enlargement of region 1 (symmetrized about the chain axis) and a schematic illustration depicting alternating arrangement of I-2-3I-2K-I and K-2I-3K-2I-K {100} layers within the crystal. The lower right inset shows the surface plot of region 1. (**B** to **F**) Single-pixel line profiles obtained from line traces marked B to F in the upper left inset in (A). The background level in these profiles is arbitrary because the reconstruction procedure does not recover low-spatial-frequency variations in phase. Schematic crystal structures showing atoms contributing to the contrast are also shown.

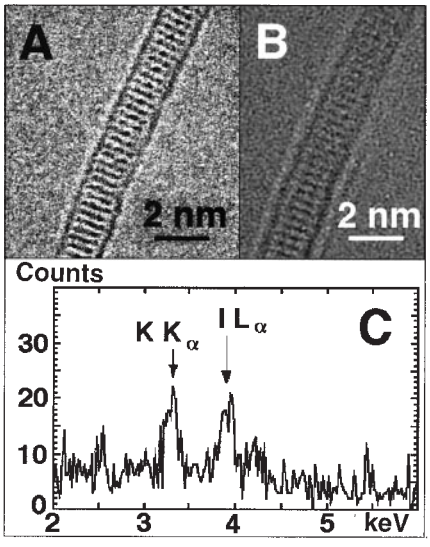

Fig. 2. (**A**) Unprocessed Scherzer defocus HRTEM image from the focal series used to generate Fig. 1A. Intensity is ~3000 counts in vacuum. (**B**) Reconstructed amplitude image (black = 0.9, white = 1.1, amplitude in vacuum = 1). (**C**) EDX spectrum obtained from a filled nanotube using a 5-nm-diameter probe.

sion and a distortion from the expected square lattice (with a larger expansion along <100> than along <110>). Although an apparent distortion could also be generated by a tilt of the crystal by ~9.7°, a tilt of this magnitude cannot be present because the measured defocus difference along the tube is only 1.75 nm. A tilt about the tube axis can also be discounted because it would lead to asymmetry in the Fourier transform of the reconstructed exit surface wave function, which is not observed experimentally. The average distortion is approximately consistent with the Poisson ratio of 0.293 measured for bulk KI (*23*). It is likely to result from the adaptation of the crystal to the radially symmetrical van der Waals surface of the confining SWNT. In addition, in bulk KI, the lattice coordination is 6:6, and each ion is surrounded by six nearest neighbors of opposite charge, whereas in the SWNT-incorporated three-layer crystal, only the central . . .K-I-K-I. . . row has 6:6 coordination, and the face and edge atoms have reduced coordinations of 5:5 and 4:4, respectively. The observed distortion may provide a reduction in lattice energy associated with the alleviation of Coulomb interactions within the three-layer crystal as compared to those in bulk KI.

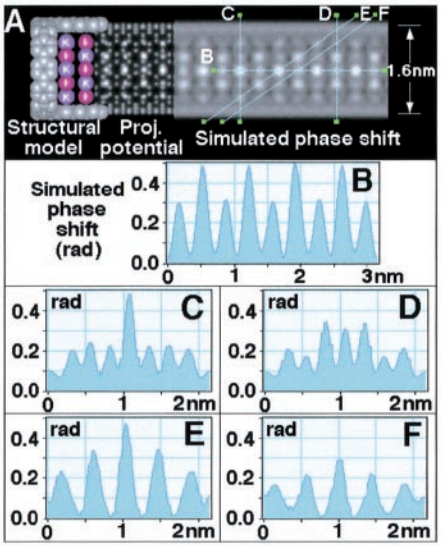

Fig. 3. (**A**) Composite diagram showing the structural model, projected potential, and simulated phase image for a <110> projection of a KI crystal that is three atomic layers thick and confined within a (12,12) SWNT. (**B** to **F**) Single-pixel line profiles obtained from line traces marked B to F in (A).

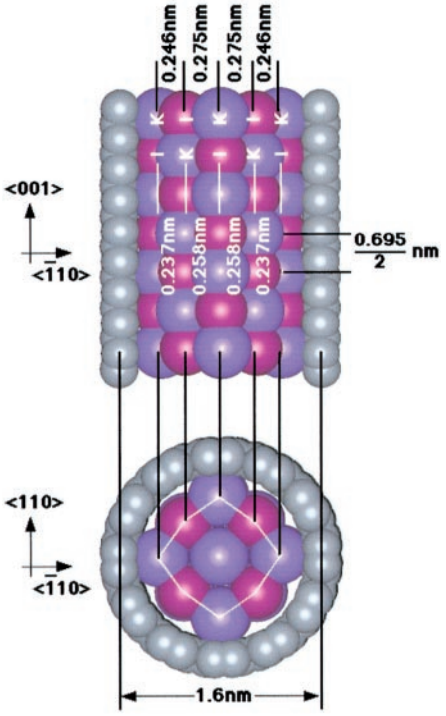

Fig. 4. Structural model corresponding to physical measurements obtained from the image in Fig. 1A. Upper and lower sections show the <110> projection and cross section, respectively, of the KI crystal in a (12,12) SWNT. Estimated precision of measurements, ±0.003 nm.

We have performed similar measurements on KI crystals encapsulated within SWNTs that have diameters other than 1.6 nm. Several strain states of the confined KI crystals, which are related directly to SWNT diameter, have been observed. Our results show that if the diameter of a SWNT can be preselected, then it can be used to template particular strain states of encapsulated 1D crystals and to thereby tailor their physical properties. Fiske and Coleman have shown how the longitudinal-optical phonon behavior of ultrathin films of RbI, KI, and CsI varies as a function of crystal thickness and how the mode strength of RbI decreases as the crystal thickness approaches the scale described in this study (*24*). The properties of single crystals of materials other than metal halides may be modified in a similar manner. It is particularly exciting that, within SWNTs, we have also successfully encapsulated materials [such as silver (*1*)] that are metallic in their bulk form.

References and Notes

1. J. Sloan *et al.*, *J. Chem. Soc. Chem. Commun.* **1999**, 699 (1999).
2. Y. Kondo and K. Takayanagi, *Phys. Rev. Lett.* **79**, 3455 (1997).
3. L. D. Marks and D. J. Smith, *Nature* **303**, 316 (1983).
4. L. D. Marks, V. Heine, D. J. Smith, *Phys. Rev. Lett.* **52**, 656 (1984).
5. S. Iijima, *Optik* **48**, 193 (1977).
6. J. L. Hutchison and N. A. Briscoe, *Ultramicroscopy* **18**, 435 (1985).
7. W. Coene, G. Janssen, M. Op de Beeck, D. Van Dyck, *Phys. Rev. Lett.* **69**, 3743 (1992).
8. D. Van Dyck, M. Op de Beeck, W. Coene, *Optik* **93**, 103 (1993).
9. W. Coene, A. Thust, M. Op de Beeck, D. Van Dyck, *Ultramicroscopy* **64**, 109 (1996).
10. A. I. Kirkland, W. O. Saxton, K. L. Chau, K. Tsuno, M. Kawasaki, *Ultramicroscopy* **57**, 355 (1995).
11. A. I. Kirkland, W. O. Saxton, G. Chand, *J. Electron Microsc.* **1**, 11 (1997).
12. A. Tonomura, *Phys. Rev. Lett.* **69**, 293 (1992).
13. D. Van Dyck, in *Electron Microscopy in Materials Science*, U. Valdre, Ed. (Academic Press, New York, 1992), p. 193.
14. C. Journet *et al.*, *Nature* **388**, 756 (1997).
15. The KI was ground together with the SWNTs in an agate mortar and pestle, placed in an evacuated silica quartz ampoule, heated at 2 K min^{-1} to 954 K, held at this temperature for 2 hours, and then furnace-cooled to room temperature. The product was dispersed in Analar chloroform and placed dropwise onto a holey carbon support grid.
16. J. L. Hutchison, R. C. Doole, R. E. Dunin-Borkowski, J. Sloan, M. L. H. Green, *JEOL News* **34E**, 10 (1999).
17. A. I. Kirkland, R. E. Dunin-Borkowski, J. L. Hutchison, W. O. Saxton, *Inst. Phys. Conf. Ser.* **161**, 259 (1999).
18. The microscope has a spherical aberration coefficient of 0.57 mm and a point resolution of 0.16 nm. EDX spectra were recorded from discrete SWNTs by using an Oxford Instruments ISIS 300 system with a 5-nm-diameter probe. Images of filled nanotubes located over holes in the carbon support film were acquired at a magnification of ×600,000 using a 1024-pixel Gatan 794 charge-coupled device camera. The microscope alignment was corrected for axial coma and twofold astigmatism with power spectra obtained from amorphous regions of the carbon support film. Six images of the support film (two axial and four with orthogonal tilts) were used to determine that the threefold astigmatism coefficient of the microscope is 855 nm. This value was used in the restoration. The magnification was calibrated with a Si<110> crystal.
19. The focal increment between images was 8 nm, and the exposure time for each image was 1 s. A final image with the same nominal defocus as the initial image was obtained to assess the extent of beam damage. The images were processed with a method for crystalline materials that have insufficient amorphous material to allow aberration determination by conventional means. Relative defocus values and initial registration vectors were determined with a 300-pixel area adjacent to the nanotube. Because of different drift rates for different regions of the nanotube, registration vectors were found for 12 small overlapping subregions. For each subregion, an initial restored wave function was calculated. The positional alignment was then refined, and the absolute defocus and astigmatism were determined for each region by using the phase correlation index [R. R. Meyer, A. I. Kirkland, W. O. Saxton, *Inst. Phys. Conf. Ser.* **161**, 295 (1999)]. The defocus values of the nanotube itself (and the independently determined value of the threefold astigmatism) were used to produce restorations that included a deconvolution of the modulation transfer function of the detector [R. R. Meyer and A. I. Kirkland, *Microsc. Res. Tech.* **49**, 269 (2000)]. The subregions were combined to give the final restoration shown in Fig. 1A.
20. The conformation of a SWNT can be expressed as two integers (*n*, *m*) in the equation $\mathbf{C}_h = n\mathbf{a}_1 + m\mathbf{a}_2$, where $\mathbf{a}_1$ and $\mathbf{a}_2$ are the basal vectors of the parent two-dimensional carbon lattice and $\mathbf{C}_h$ is a "roll-up" vector [M. S. Dresselhaus, G. Dresselhaus, R. Saito, *Carbon* **33**, 883 (1995)].
21. C. B. Boothroyd, *J. Microsc.* **190**, 99 (1998).
22. M. Ahtee, *Ann. Acad. Sci. Fenn. Ser. A6 Phys.* **313**, 1 (1969).
23. G. Simmons and H. Wang, *Single Crystal Elastic Constants and Calculated Aggregate Properties* (MIT Press, Cambridge, MA, ed. 2, 1971).
24. T. G. Fiske and L. B. Coleman, *Phys. Rev. B* **45**, 1414 (1992).

25. We thank W. O. Saxton, G. Brown, S. Friedrichs, C. Xu, V. C. Williams, K. S. Coleman, A. P. E. York, E. Flahaut, and R. L. Callender for contributions to this work, which was supported by the Petroleum Research Fund administered by the American Chemical Society (grant 33765-AC5), the Engineering and Physical Sciences Research Council (grants GR/L59238, GR/L22324, and GR/L10680), JEOL, and Colebrand.

3 May 2000; accepted 23 June 2000